

JOintGS: Joint Optimization of Cameras, Bodies and 3D Gaussians for In-the-Wild Monocular Reconstruction

Zihan Lou ^{*1} Jinlong Fan ^{*2} Sihan Ma ³ Yuxiang Yang ² Jing Zhang ^{1†}

Abstract

Reconstructing high-fidelity animatable 3D human avatars from monocular RGB videos remains challenging, particularly in unconstrained in-the-wild scenarios where camera parameters and human poses from off-the-shelf methods (e.g., COLMAP, HMR2.0) are often inaccurate. Splatting (3DGS) advances demonstrate impressive rendering quality and real-time performance, they critically depend on precise camera calibration and pose annotations, limiting their applicability in real-world settings. We present **JOintGS**, a unified framework that jointly optimizes camera extrinsics, human poses, and 3D Gaussian representations from coarse initialization through a *synergistic refinement mechanism*. Our key insight is that explicit foreground-background disentanglement enables mutual reinforcement: static background Gaussians anchor camera estimation via multi-view consistency; refined cameras improve human body alignment through accurate temporal correspondence; optimized human poses enhance scene reconstruction by removing dynamic artifacts from static constraints. We further introduce a temporal dynamics module to capture fine-grained pose-dependent deformations and a residual color field to model illumination variations. Extensive experiments on NeuMan and EMDB datasets demonstrate that JOintGS achieves superior reconstruction quality, with 2.1 dB PSNR improvement over state-of-the-art methods on NeuMan dataset, while maintaining real-time rendering. Notably, our method shows significantly enhanced robustness to noisy initialization compared to the baseline. Our source code is available at <https://github.com/MiliLab/JOintGS>.

^{*}Equal contribution [†] Corresponding author. ¹School of Computer Science, Wuhan University, China ²Hangzhou Dianzi University, China ³Nanyang Technological University, Singapore. Correspondence to: Jing Zhang <jingzhang.cv@gmail.com>.

Preprint. February 5, 2026.

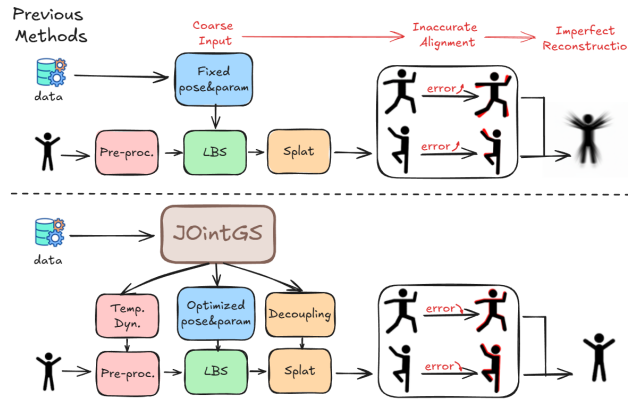


Figure 1. Comparison with Previous Methods. Unlike existing approaches that assume fixed camera poses and SMPL parameters as inputs, our JOintGS performs unified joint optimization through a synergistic refinement mechanism.

1. Introduction

Reconstructing high-fidelity, animatable 3D human avatars from monocular videos has emerged as a fundamental challenge in computer vision with broad applications in virtual reality, telepresence, digital entertainment, and human-computer interaction (Wang et al., 2024). Recent advances in neural rendering, particularly 3D Gaussian Splatting (3DGS) (Kerbl et al., 2023), have demonstrated unprecedented rendering quality and efficiency, enabling real-time photorealistic synthesis. Building upon this success, several methods (Qian et al., 2024b; Moon et al., 2024; Guo et al., 2025; Hu et al., 2024b; Guo et al., 2023; Kocabas et al., 2024; Zhang et al., 2025; Li et al., 2024a; Shao et al., 2024) have extended 3DGS to dynamic human reconstruction, achieving impressive results on controlled datasets with multi-view captures or precisely calibrated cameras.

However, these methods face a fundamental limitation when applied to *in-the-wild* monocular videos: they critically depend on highly accurate camera parameters and human pose annotations to maintain consistent spatial-temporal alignment. This dependency severely limits practical applicability, as obtaining such precise estimates remains notoriously challenging in unconstrained settings. Traditional Structure-from-Motion (SfM) pipelines like COLMAP (Schönberger

& Frahm, 2016; Schönberger et al., 2016) often struggle with dynamic scenes, producing noisy camera trajectories due to insufficient static feature correspondences. Similarly, monocular human pose estimators (Shan et al., 2022; Xu et al., 2023; Zhang et al., 2023; Cai et al., 2023; Goel et al., 2023), while achieving impressive 2D keypoint detection, frequently yield inaccurate 3D SMPL parameters due to depth ambiguity and occlusions. Even modest errors in these prerequisites cascade into severe artifacts such as inaccurate alignment, temporal inconsistencies, and unrealistic human-scene interpenetration.

The key insight is that while obtaining precise camera and pose parameters is difficult, coarse estimates are readily derived. Rather than treating these initial estimates as fixed ground truth, we pose a central question: *Can we leverage the rich geometric and photometric constraints inherent in 3DGS-based reconstruction to jointly refine camera trajectories, human poses, and 3D representations?* This question motivates our proposed framework, **JOintGS**, which formulates dynamic human reconstruction as a unified optimization problem.

JOintGS introduces a *synergistic refinement mechanism* through explicit foreground-background disentanglement, where different components mutually reinforce each other through three complementary pathways: (1) Static background Gaussians, remaining consistent across frames, naturally provide multi-view geometric constraints for camera pose estimation. By exploiting photometric consistency on static regions, we progressively refine camera trajectories without being affected by dynamic human motion; (2) With refined cameras establishing accurate spatial-temporal correspondences, we optimize human poses to minimize re-projection errors of human silhouettes and appearance, correcting initialization errors from monocular pose estimators; (3) Improved camera and poses enhance human-scene disentanglement by providing accurate foreground-background separation. Clean background constraints, in turn, stabilize camera estimation by removing dynamic artifacts that violate static scene assumptions. Unlike previous methods that either treat camera and pose as fixed inputs or optimize them separately (Jiang et al., 2023; Hu et al., 2024a) (Figure 1), our approach forms a closed-loop system where each component progressively corrects errors in the others. This synergistic design enables robust reconstruction from coarse initialization without requiring pre-calibrated inputs or expensive preprocessing.

Furthermore, to effectively model the complex dynamics of human motion, we introduce two complementary components: a temporal offset module that learns per-frame non-rigid geometric deformations to capture fine-grained changes like clothing wrinkles, and a residual color field that models appearance variations caused by lighting changes

and view-dependent effects. These modules enable our method to faithfully reconstruct both geometric and photometric details that are challenging to capture with canonical representations alone (Weng et al., 2022; Hu et al., 2024a; Qian et al., 2024b).

We perform comprehensive evaluations on two challenging in-the-wild datasets, NeuMan (Jiang et al., 2022) and EMDB (Kaufmann et al., 2023). Experimental results show that JOintGS delivers superior reconstruction quality, achieving a 2.2 dB PSNR improvement over SOTA approaches on the NeuMan dataset, while maintaining real-time rendering performance. Furthermore, JOintGS demonstrates stronger robustness to noisy initialization, exhibiting only a 0.9 dB PSNR drop at $\sigma=0.01$, in contrast to the 3.7 dB drop observed with the strong baseline HUGS (Kocabas et al., 2024). Comprehensive ablation studies further confirm the necessity of the joint optimization strategy and the effectiveness of each component in our synergistic refinement mechanism.

In summary, our main contributions are:

- We propose **JOintGS**, a unified framework jointly optimizing camera trajectories, human poses, and 3D Gaussians from coarse initialization, enabling robust, calibration-free reconstruction and achieving SOTA performance.
- We introduce a **synergistic refinement mechanism** through explicit foreground-background disentanglement, where static backgrounds anchor camera optimization, refined cameras improve human body alignment, and optimized poses enhance scene reconstruction, forming a closed-loop of mutual reinforcement.
- We design efficient **temporal offset and residual modules** capturing fine-grained deformations and appearance variations while maintaining real-time rendering.

2. Related Work

NeRF-based Human Reconstruction. Neural radiance fields have enabled photorealistic human avatar reconstruction from monocular videos (Weng et al., 2022; Jiang et al., 2022; Li et al., 2024b; Guo et al., 2023; Peng et al., 2023; Feng et al., 2022; Mihajlovic et al., 2022; Liu et al., 2021). These methods achieve impressive quality by mapping posed observations to canonical space via SMPL-guided deformations (Loper et al., 2023), but suffer from slow rendering due to expensive volume rendering. NeuMan (Jiang et al., 2022) jointly models humans and static scenes, while HumanNeRF (Weng et al., 2022) focuses on human-only reconstruction. However, both assume fixed camera poses, limiting applicability to in-the-wild scenarios where pre-calibrated cameras are unavailable.

3DGS-based Human Reconstruction. Recent advances in 3D Gaussian Splatting (3DGS) (Kerbl et al., 2023) offer fast alternatives through explicit point-based representations. GaussianAvatar (Hu et al., 2024a) binds 3D Gaussians to SMPL vertices with pose-dependent appearance modeling via hash-encoded MLPs, achieving real-time rendering. 3DGS-Avatar (Qian et al., 2024b) explicitly models non-rigid deformations and pose-dependent color changes with MLPs, achieving high-fidelity reconstruction at the cost of increased training time. HUGS (Kocabas et al., 2024) jointly models humans and scenes using 3D Gaussians but lacks mechanisms for correcting initialization errors. Most existing methods critically depend on pre-calibrated cameras and accurate SMPL parameters as fixed inputs, which are difficult to obtain in real-world scenarios.

Holistic Human-Scene Reconstruction. Several methods attempt holistic reconstruction of both humans and scenes. Vid2Avatar (Guo et al., 2023) employs a human-centric scene model but struggles with proper multi-view geometry learning. HSR (Xue et al., 2024) extends Vid2Avatar with scene fields and holistic representation but shows degraded performance in outdoor scenes. ODHSR (Zhang et al., 2025) proposes an online dense reconstruction framework, achieving impressive results through monocular geometric priors. However, their online updating strategy processes frames sequentially, potentially missing global optimization opportunities available when the full sequence is accessible.

Joint Camera and Pose Optimization. Traditional bundle adjustment (Triggs et al., 1999) jointly optimizes camera poses and 3D structure but struggles with dynamic scenes. Recent learning-based methods incorporate human priors into structure-from-motion. HSfM (Müller et al., 2025) integrates human reconstruction into classic SfM, demonstrating that modeling humans improves camera pose accuracy. PoseDiffusion (Wang et al., 2023) uses diffusion-aided bundle adjustment for pose estimation. Unlike these methods that operate on sparse features or separate optimization stages, *our approach performs synergistic refinement within a unified differentiable rendering framework*, where dense photometric constraints from 3DGS enable tighter coupling between camera, pose, and appearance optimization.

3. Method

3.1. Overview

Given a monocular RGB video $\{\mathbf{I}_t\}_{t=1}^T$ with coarse camera poses $\{\hat{\mathbf{T}}_t = [\hat{\mathbf{R}}|\hat{\mathbf{t}}]\}$ from COLMAP (Schönberger & Frahm, 2016; Schönberger et al., 2016) and initial SMPL parameters $\{\hat{\xi}_t = (\hat{\theta}_t, \hat{\beta})\}$ from HMR2.0 (Zhang et al., 2023; Cai et al., 2023; Goel et al., 2023), our goal is to reconstruct a high-fidelity animatable human avatar and scene while simultaneously refining the camera pose and

SMPL parameters. As illustrated in Figure 2, our joint optimization framework consists of four key components: (1) *Foreground human representation* (§3.2) that models the avatar in canonical space with pose-driven deformation and temporal dynamics; (2) *Background scene representation* (§3.3) using static 3D Gaussians; (3) *Synergistic refinement mechanism* (§3.4) that simultaneously refines cameras, SMPL parameters, and Gaussian fields through unified differentiable rendering supervision.

3.2. 3D Human Representation

To model the dynamic human body with temporal variations, we represent the avatar as a collection of 3D Gaussians $\mathcal{G}_H = \{\mathbf{g}_i^H\}_{i=1}^{N_H}$ defined in a canonical space and deformed to arbitrary poses via learned skinning.

3.2.1. CANONICAL GAUSSIAN FIELD

Following recent advances in Gaussian-based avatars (Kocabas et al., 2024; Hu et al., 2024b), we establish a *canonical space* corresponding to SMPL rest pose (e.g., A-pose). Each human Gaussian \mathbf{g}_i^H is parameterized by its canonical attributes: center position $\boldsymbol{\mu}_i^c \in \mathbb{R}^3$, rotation $\mathbf{R}_i^c \in SO(3)$, scale $\mathbf{S}_i^c \in \mathbb{R}_+^3$, opacity $\alpha_i \in [0, 1]$, SH coefficients \mathbf{c}_i , and learned LBS weights $\mathbf{w}_i \in \mathbb{R}^K$. These canonical attributes are decoded from features sampled on a Triplane representation. We initialize \mathcal{G}_H by uniformly sampling $N_H=110k$ points on the SMPL mesh in the canonical pose. Each Gaussian inherits LBS weights $\mathbf{w}_i \in \mathbb{R}^K$ from its nearest SMPL vertex via barycentric interpolation, where $K=24$ denotes the number of joints.

3.2.2. POSE-DRIVEN DEFORMATION

To render canonical Gaussians under pose $\boldsymbol{\theta}_t$ at frame t , we apply standard LBS deformation (Jung et al., 2023; Li et al., 2024b; Pang et al., 2024). Given SMPL parameters $(\boldsymbol{\theta}_t, \boldsymbol{\beta})$ and per-joint transformation matrices $\{\mathcal{T}_k^t \in SE(3)\}_{k=1}^K$ computed via forward kinematics, we transform each Gaussian’s attributes as:

$$\boldsymbol{\mu}_i^t = \sum_{k=1}^K w_{i,k} \mathcal{T}_k(\boldsymbol{\theta}_t) \begin{bmatrix} \boldsymbol{\mu}_i^c \\ 1 \end{bmatrix}, \quad (1)$$

$$\mathbf{R}_i^t = \left(\sum_{k=1}^K w_{i,k} \mathbf{R}_k(\boldsymbol{\theta}_t) \right) \mathbf{R}_i^c, \quad (2)$$

where $[\boldsymbol{\mu}_i^c; 1]$ denotes homogeneous coordinates and $\mathbf{R}_k(\boldsymbol{\theta}_t) = \mathcal{T}_k(\boldsymbol{\theta}_t)_{3:3}$ extracts the rotation component. We blend only rotational components for orientation to maintain shape consistency (Qian et al., 2024a). The covariance is updated as $\boldsymbol{\Sigma}_i^t = \mathbf{R}_i^t \mathbf{S}_i^c (\mathbf{S}_i^c)^\top (\mathbf{R}_i^t)^\top$.

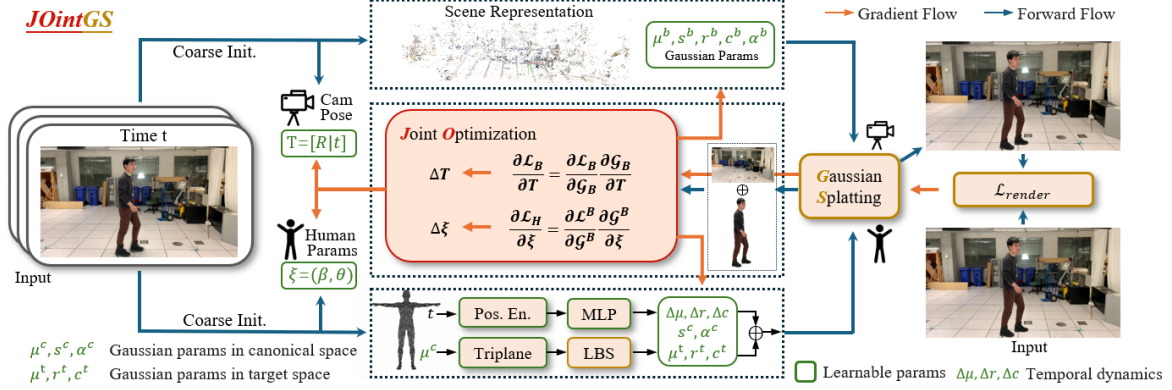


Figure 2. JOintGS Framework Overview. Given a monocular RGB video with coarse camera poses $\mathbf{T} = [\mathbf{R}|t]$ from COLMAP and initial SMPL parameters $\xi = (\beta, \theta)$ from HMR2.0, we initialize scene Gaussians \mathcal{G}_B (from COLMAP point cloud) and human Gaussians \mathcal{G}_H (from SMPL vertices) in canonical space. Our synergistic refinement mechanism (highlighted by orange gradient flow) jointly optimizes camera pose corrections $\Delta\mathbf{T}$, SMPL parameter refinements $\Delta\xi$, and Gaussian attributes $\{\mathcal{G}_H, \mathcal{G}_B\}$ through unified differentiable rendering supervision. The optimization operates through three complementary pathways: (1) **Background-anchored camera refinement**: static scene Gaussians provide multi-view geometric constraints via photometric loss \mathcal{L}_B on background regions; (2) **Camera-guided human optimization**: refined cameras enable accurate temporal correspondence for SMPL parameter optimization via human rendering loss \mathcal{L}_H ; (3) **Pose-aware Gaussian optimization**: improved camera and SMPL parameters enhance foreground-background disentanglement, facilitating Gaussian field optimization with photometric losses $\mathcal{L}_{\text{render}}$. This closed-loop mutual refinement enables robust reconstruction from noisy initialization without requiring pre-calibrated inputs.

3.2.3. TEMPORAL DYNAMICS MODELING

While LBS-based deformation handles skeletal articulation, it cannot capture *non-rigid dynamics* such as clothing wrinkles and *appearance variations* caused by motions and lighting. To address this limitation, we introduce two lightweight modules that model residual deformations and appearance changes beyond the skeletal motion:

Temporal Offset Module. We model per-frame non-rigid geometric deformations via a shallow MLP $\mathcal{F}_{\text{offset}}$. It predicts positional and rotational offsets conditioned on the canonical position μ_i^c and the encoded frame index t :

$$[\Delta\mu_i^t, \Delta\mathbf{R}_i^t] = \mathcal{F}_{\text{offset}}(\mathcal{E}(\mu_i^c), \gamma(t)), \quad (3)$$

where $\mathcal{E}(\cdot)$ denotes multi-resolution hash encoding (Müller et al., 2022) and $\gamma(\cdot)$ denotes positional encoding (Vaswani et al., 2017). The final posed position and rotation incorporate these offsets by:

$$\mu_i^t \leftarrow \mu_i^t + \Delta\mu_i^t, \quad \mathbf{R}_i^t \leftarrow \mathbf{R}_i^t \cdot \Delta\mathbf{R}_i^t. \quad (4)$$

Temporal Color Module. To model temporal appearance variations (e.g., shadows, lighting changes), we predict a per-Gaussian color residual via another MLP $\mathcal{F}_{\text{color}}$, which is added to the base spherical harmonics color during rendering:

$$\mathbf{c}_i^t(\mu_i^c) = \mathbf{c}_i^{\text{SH}}(\mu_i^c) + \mathcal{F}_{\text{color}}(\mathcal{E}(\mu_i^c), \gamma(t)). \quad (5)$$

These modules are regularized to remain small (see §3.5), ensuring they capture only the residual dynamics beyond skeletal motion.

3.3. Background Scene Representation

We represent the static scene as a set of 3D Gaussians, denoted as $\mathcal{G}_B = \{\mathbf{g}_i^B\}_{i=1}^{N_B}$, where each Gaussian is characterized by a center position $\mu_i \in \mathbb{R}^3$, a 3D covariance matrix Σ_i , an opacity $\alpha_i \in [0, 1]$, and a view-dependent color parameterized by SH coefficients. We initialize \mathcal{G}_B from the sparse point cloud reconstructed by COLMAP, which typically contains between 10k and 50k points, depending on the scene complexity. The initial Gaussian scales are set proportionally to the local point density, while their colors are inherited from the nearest image observations.

3.4. Synergistic Refinement Mechanism

The core innovation of our method lies in the *synergistic refinement* of three interdependent components, camera poses $\{\mathbf{T}_t\}$, SMPL parameters $\{(\theta_t, \beta)\}$, and Gaussian fields $\{\mathcal{G}_H, \mathcal{G}_B\}$, within a unified differentiable rendering framework. Unlike prior works that optimize these components separately (Qian et al., 2024a) or assume pre-calibrated inputs (Jiang et al., 2023; Xu et al., 2024), our approach exploits their mutual dependencies through a closed-loop refinement process where each component progressively corrects errors in the others. To establish a unified world coordinate system, we employ RANSAC (Fischler & Bolles, 1981) to fit scale-shift parameters, aligning SMPL depths to COLMAP’s metric scale following.

This synergy operates through three complementary pathways that form a closed-loop of mutual reinforcement:

Background-Anchored Camera Refinement. Static background Gaussians \mathcal{G}_B provide reliable multi-view geometric constraints across frames. Given initial camera pose $\hat{\mathbf{T}}_t$ from COLMAP, we parameterize a learnable correction:

$$\mathbf{T}_t = \Delta \mathbf{T}_t \circ \hat{\mathbf{T}}_t, \quad (6)$$

where $\Delta \mathbf{T}_t \in \text{SE}(3)$ is represented via axis-angle and translation. We optimize $\Delta \mathbf{T}_t$ by minimizing photometric errors on static regions identified using human masks \mathbf{M}_t from SAM (Kirillov et al., 2023; Ravi et al., 2024):

$$\mathcal{L}_B = \|(1 - \mathbf{M}_t) \odot (\mathbf{I}_t - \hat{\mathbf{I}}_t^B)\|_1, \quad (7)$$

where $\hat{\mathbf{I}}_t^B$ is rendered from \mathcal{G}_B and \odot denotes element-wise multiplication. By isolating camera optimization from dynamic human motion, this strategy prevents artifacts from violating temporal consistency constraints.

Camera-Guided Human Pose Optimization. With refined cameras establishing accurate spatial-temporal correspondences, we optimize SMPL parameters $\{(\theta_t, \beta)\}$ through photometric and silhouette supervision:

$$\mathcal{L}_H = \|\mathbf{M}_t \odot (\mathbf{I}_t - \hat{\mathbf{I}}_t^H)\|_1 + \|\mathbf{M}_t - \hat{\mathbf{M}}_t^H\|_1, \quad (8)$$

where $\hat{\mathbf{I}}_t^H$ and $\hat{\mathbf{M}}_t^H$ are rendered from \mathcal{G}_H . Improved camera alignment enables gradients from these losses to flow directly to SMPL parameters via the differentiable LBS transformation (Eq. 1–2), correcting initialization errors from monocular pose estimators.

Pose-Aware Gaussian Optimization. Refined camera and SMPL parameters enhance foreground-background disentanglement by providing accurate skeletal priors. This reduces foreground leakage into \mathcal{G}_B and eliminates background artifacts from \mathcal{G}_H . We optimize Gaussian parameters using photometric losses:

$$\mathcal{L}_{\text{render}} = \lambda_{\text{rgb}} \mathcal{L}_{\text{rgb}} + \lambda_{\text{ssim}} \mathcal{L}_{\text{ssim}} + \lambda_{\text{lpips}} \mathcal{L}_{\text{lpips}}, \quad (9)$$

where $\mathcal{L}_{\text{rgb}} = \|\mathbf{I}_t - \hat{\mathbf{I}}_t\|_1$ is ℓ_1 loss, $\mathcal{L}_{\text{ssim}}$ (Wang et al., 2004) measures structural similarity, and $\mathcal{L}_{\text{lpips}}$ (Zhang et al., 2018) captures perceptual quality. Cleaner scene separation further stabilizes camera estimation by removing dynamic motion from static constraints, completing the feedback loop.

3.5. Training Strategy and Objectives

We employ a structured **three-stage** optimization schedule to prevent degenerate solutions and ensure stable convergence. (i) *Warm-up*: We optimize only Gaussian parameters $\{\mathcal{G}_H, \mathcal{G}_B\}$ with fixed camera and SMPL parameters, establishing a reliable geometry prior before moving to pose-related updates. (ii) *Independent Optimization*: We simultaneously enable the optimization of camera poses and SMPL parameters $\{(\theta_t, \beta)\}$. During this stage, these

components are updated independently to avoid gradient interference: cameras are primarily anchored by static background cues for multi-view consistency, while SMPL parameters are refined to correct pose initialization errors based on human-centric gradients. (iii) *Joint Optimization*: We perform full optimization with complete losses, allowing for **synergistic refinement** where camera trajectories, body poses, and Gaussian attributes mutually correct each other to achieve global consistency. More details are provided in the supplementary material.

To prevent overfitting and maintain generalization, we introduce extra complementary regularizations. *LBS weight regularization* constrains learned weights to remain close to SMPL initialization:

$$\mathcal{L}_{\text{lbs}} = \sum_{i=1}^{N_H} \|\mathbf{w}_i - \mathbf{w}_i^{\text{SMPL}}\|_2^2, \quad (10)$$

preventing skinning weights from overfitting to training poses. *Offset regularization* penalizes large deformations to ensure temporal modules capture only residual dynamics:

$$\mathcal{L}_{\text{offset}} = \sum_{i=1}^{N_H} \sum_{t=1}^T (\|\Delta \boldsymbol{\mu}_i^t\|_2^2 + \|\Delta \mathbf{R}_i^t - \mathbf{I}\|_F^2 + \|\Delta \mathbf{c}_i^t\|_2^2), \quad (11)$$

where \mathbf{I} is the identity rotation. *Canonical regularization* softly anchors human Gaussians near SMPL mesh surface:

$$\mathcal{L}_{\text{canonical}} = \sum_{i=1}^{N_H} \min_{j \in \{1, \dots, N_v\}} \|\boldsymbol{\mu}_i^c - \bar{\mathbf{v}}_j\|_2^2, \quad (12)$$

where $\{\bar{\mathbf{v}}_j\}$ are canonical SMPL vertices.

4. Experiments

We conduct comprehensive experiments to evaluate the effectiveness of our proposed method. We first describe the datasets and evaluation metrics (§4.1), followed by implementation details (§4.2). We then present quantitative (§4.3) and qualitative (§4.4) comparisons with state-of-the-art methods. Finally, ablation studies validate the design choices of our key components (§4.5).

4.1. Dataset

NeuMan Dataset (Jiang et al., 2022) comprises six in-the-wild sequences (Seattle, Citron, Parking, Bike, Jogging, Lab), each capturing a single person performing various activities over 10–20 seconds. The videos are recorded with a handheld mobile phone exhibiting natural camera motion, which provides sufficient viewpoint diversity for multi-view reconstruction. We follow the original split protocol (Jiang et al., 2022), allocating 80% of frames for training, 10% for validation, and 10% for testing. Notably, we *do not* use the

Method	Human-only			Full-image		
	PSNR↑	SSIM↑	LPIPS↓	PSNR↑	SSIM↑	LPIPS↓
Vid2Avatar (Guo et al., 2023)	30.96	0.981	0.018	15.64	0.551	0.572
HUGS (Kocabas et al., 2024)	30.13	0.977	0.017	26.66	0.851	0.126
HSR (Xue et al., 2024)	29.03	0.971	0.026	21.67	0.669	0.526
ODHSR (Zhang et al., 2025)	32.07	0.981	0.016	27.78	0.870	0.153
ExAvatar (Moon et al., 2024)	31.39	0.981	0.016	-	-	-
Vid2Avatar-Pro (Guo et al., 2025)	32.71	0.983	0.019	-	-	-
JOintGS (Ours)	34.84	0.984	0.010	30.23	0.913	0.072

Table 1. Quantitative evaluation on NeuMan dataset (Jiang et al., 2022). We report performance on both human-only regions and entire frames (Full-image). For the **human-only** setting, we render the avatar on a white background for all baselines and compute metrics over the whole image.

Method	Human-only			Full-image		
	PSNR↑	SSIM↑	LPIPS↓	PSNR↑	SSIM↑	LPIPS↓
GauHuman (Hu et al., 2024b)	25.31	0.943	0.057	-	-	-
3DGS-Avatar (Qian et al., 2024b)	27.95	0.967	0.035	-	-	-
Vid2Avatar (Guo et al., 2023)	24.25	0.948	0.061	16.65	0.413	0.599
HUGS (Kocabas et al., 2024)	26.16	0.947	0.033	21.60	0.659	0.181
HSR (Xue et al., 2024)	25.12	0.920	0.054	18.67	0.463	0.632
ODHSR (Zhang et al., 2025)	28.95	0.966	0.031	23.79	0.767	0.197
JOintGS (Ours)	30.99	0.972	0.027	23.40	0.785	0.173

Table 2. Quantitative evaluation on EMDB dataset (Kaufmann et al., 2023). We report metrics on both human-only regions and entire frames (Full-image) to provide a multi-faceted assessment. Our method outperforms both offline and online baselines.

keyframe selection strategy on this dataset to enable direct comparison with prior offline methods. This dataset serves as our primary benchmark for quantitative evaluation.

EMDB Dataset (Kaufmann et al., 2023) is a large-scale in-the-wild dataset consisting of 81 video sequences from 10 subjects, totaling 58 minutes of motion data. The dataset is captured using Wearable trackers and a handheld iPhone, providing ground-truth global camera poses and body root trajectories via wireless motion capture sensors. We select ten representative sequences that present diverse challenges: extended trajectories, occlusions, complex lighting (shadows), and unconventional poses (*e.g.*, cartwheels). We use the first 200 frames from each sequence and adopt an 80%/10%/10% train/val/test split.

Baselines. We compare against state-of-the-art methods across different categories: (1) *NeRF-based human reconstruction*: HumanNeRF (Weng et al., 2022), InstantAvatar (Jiang et al., 2023); (2) *3DGS-based human reconstruction*: 3DGS-Avatar (Qian et al., 2024b), GaussianAvatar (Hu et al., 2024a), ExAvatar (Moon et al., 2024); (3) *Video-based human reconstruction*: Vid2Avatar (Guo et al., 2023), Vid2Avatar-Pro (Guo et al., 2025); (4) *Holistic human-scene reconstruction*: NeuMan (Jiang et al., 2022), HUGS (Kocabas et al., 2024), HSR (Xue et al., 2024), ODHSR (Zhang et al., 2025).

Evaluation Metrics. We evaluate reconstruction quality

using standard photometric metrics: PSNR, SSIM (Wang et al., 2004), and LPIPS (Zhang et al., 2018). For human-only rendering, we composite the reconstructed avatar onto a white background and compute metrics over the entire image region. We also report training time (hours) and rendering speed (FPS) to assess computational efficiency.

4.2. Implementation Details

All experiments were conducted on a single NVIDIA RTX 5090 GPU (32GB). The model was optimized using the Adam (Kinga et al., 2015) optimizer, with a stage-dependent learning rate scheduling strategy employed throughout the training process. Training converged in approximately 25 minutes over 15,000 iterations. Detailed loss weights, learning rate schedules, initialization methods, and network architectures are provided in the supplementary material.

4.3. Quantitative Results

Novel View Synthesis on NeuMan. Table 1 presents quantitative evaluation results on the NeuMan dataset. Our method achieves superior performance across all metrics, an average PSNR of 34.84 dB, surpassing the previous best Vid2Avatar-Pro (Guo et al., 2025) (32.71 dB) by 2.13 dB. Notably, 3DGS-based methods (3DGS-Avatar, GaussianAvatar, HUGS, Ours) consistently outperform NeRF-based approaches (HumanNeRF, InstantAvatar) in both quality and speed, demonstrating the advantages of explicit 3D



Figure 3. Qualitative comparison on NeuMan dataset. For each scene, we show full-body rendering (left) and zoomed-in details (right).



Figure 4. Novel Pose Synthesis And Environment Transfer. The reconstructed avatar can be animated with arbitrary poses while maintaining photorealistic appearance and seamless integration with other environments.

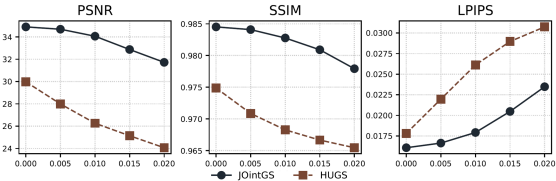


Figure 5. Robustness Comparison on noisy initialization.

Gaussian representation for human modeling. Our method also achieves highest SSIM (0.984) and LPIPS (0.010), indicating excellent structural similarity and perceptual quality.

Novel View Synthesis on EMDB. Table 2 shows results on the more challenging EMDB dataset featuring complex poses and occlusions. Our method achieves 30.99 dB PSNR, surpassing the recent online method ODHSR (Zhang et al., 2025) (28.95 dB) by 2.04 dB. Despite ODHSR’s online advantage enabling real-time tracking, our offline global

optimization leverages full sequence information for more robust reconstruction. The consistent improvements across both datasets validate the robustness and generalizability of our approach.

Efficiency Analysis. JointGS requires approximately 23 minutes for training on average, slightly faster than HUGS (25 minutes), while achieving significantly better quality (2.13 dB PSNR). Our method maintains real-time rendering at 27.3 FPS versus HUGS’s 27.5 FPS. This efficiency is attributed to our lightweight temporal offset module and residual color field.

Robustness to Initialization Errors. Figure 5 analyzes the robustness of our method to noisy initialization of camera poses and SMPL parameters. We incrementally add Gaussian noise to the initialization with standard deviations ranging from 0 to 0.02 (normalized scale). Our method exhibits significantly slower performance degradation compared to HUGS: at $\sigma=0.01$, our PSNR drops by only 0.9 dB versus HUGS’s 3.7 dB drop, demonstrating a 2.8 dB robustness advantage. This robustness is achieved through the synergistic refinement mechanism, which iteratively refines both camera and SMPL parameters within the joint optimization framework.

Background Reconstruction Results. While our background model primarily serves to provide correct context (e.g., occlusion and depth cues) and anchor camera refinement, it also yields high-quality scene reconstruction as a byproduct of joint optimization. As shown in Tables 1 and 2, our method surpasses the recent ODHSR by 2.45 dB in PSNR on the NeuMan dataset and achieves comparable performance on EMDB. Per-scene breakdowns and visual comparisons are provided in the supplementary material.

Configuration	PSNR↑	SSIM↑	LPIPS↓
w/o Synergistic	31.38	0.976	0.017
w/o Dynamics	34.23	0.983	0.011
Full Model (Ours)	34.84	0.984	0.010

Table 3. Ablation study on NeuMan dataset (average across six sequences). Each component contributes to the final performance, with synergistic refinement providing the largest gain.

4.4. Qualitative Results

Human Reconstruction Quality. Figure 3 presents qualitative comparisons of human reconstruction against NeuMan (Jiang et al., 2022) and HUGS (Kocabas et al., 2024). For each example, we show the full-body rendering (left) alongside two zoomed-in views highlighting fine-grained details. Our method demonstrates superior reconstruction quality across three key aspects:

Body Alignment. JointGS accurately aligns the reconstructed body with the ground-truth pose, avoiding the misalignment artifacts visible in baseline methods. This is achieved through our synergistic optimization of camera poses, SMPL parameters, and Gaussian representations.

Detail Preservation. The zoomed-in regions reveal that our method preserves fine-grained details such as facial features, clothing wrinkles, and hand gestures more faithfully than baselines. This benefit stems from the temporal offset module, which captures high-frequency deformations beyond SMPL’s rigid skeletal deformations.

Color Fidelity. Our reconstructions exhibit more accurate color reproduction compared to HUGS, which suffers from color bleeding between human and scene. The clean separation is enabled by our synergistic refinement mechanism, which refines SMPL parameters to reduce ambiguity in human-scene decomposition.

Novel Pose and Environment Transfer. As shown in Figure 4, our method enables decoupling of human and background, facilitating novel view synthesis and avatar manipulation. We demonstrate this capability by transferring a reconstructed human avatar from the Lab sequence to the Parking sequence environment, and rendering it under a novel pose extracted from a different subject. The results exhibit realistic appearance and consistent geometry, validating that JointGS effectively separates human from the background while maintaining animatable canonical representations.

4.5. Ablation Experiments

We conduct ablation studies to validate the contribution of each proposed component on the NeuMan dataset (Table 3 and Figure 6). Removing the *temporal dynamics*

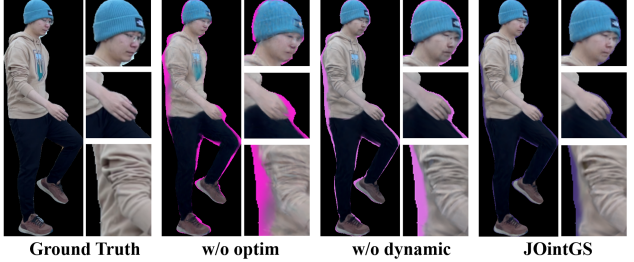


Figure 6. Qualitative visualization of the details captured in the human body reconstruction under different ablations of our method.

module (w/o Dynamics) results in a 0.6 dB PSNR drop with visible degradation in high-frequency details such as clothing wrinkles and facial features, validating its necessity for capturing pose-dependent non-rigid deformations beyond SMPL’s skeletal articulation. More critically, removing *synergistic refinement* (w/o Synergistic)—which jointly optimizes cameras, SMPL parameters, and Gaussians—leads to a substantial 3.5 dB degradation with severe artifacts including misaligned limbs and blurred textures, demonstrating that correcting initialization errors through mutual reinforcement is essential for accurate reconstruction. Our full model achieves 34.84 dB PSNR on average, confirming that geometric refinement (temporal offsets), appearance modeling (residual colors), and holistic optimization (synergistic mechanism) work synergistically to enable high-fidelity reconstruction from coarse initialization.

5. Conclusion

We present **JointGS**, a unified framework for holistic reconstruction of dynamic humans and static scenes from monocular RGB videos through synergistic refinement of camera poses, SMPL parameters, and 3D Gaussian fields. By exploiting their mutual dependencies within a differentiable rendering pipeline, our method enables robust reconstruction from coarse initialization without demanding precise pre-calibration. Extensive experiments on diverse in-the-wild datasets demonstrate that JointGS achieves state-of-the-art performance, while maintaining real-time rendering. Comprehensive ablation studies validate the effectiveness of each proposed component, particularly the synergistic refinement mechanism.

Limitations. Our approach is fundamentally constrained by the inherent capacity of the SMPL body model, leading to reduced fidelity in fine-grained regions such as hands and faces. Although our temporal dynamics module exhibits a tendency to capture residual detail in these areas, a promising future direction is to improve hand and face modeling and enhance the controllability of expressions and gestures by integrating more expressive parametric models (Shen et al., 2023), such as SMPL-X (Pavlakos et al., 2019).

Impact Statement

This paper presents work whose goal is to advance the field of Machine Learning. There are many potential societal consequences of our work, none of which we feel must be specifically highlighted here.

References

Cai, Z., Yin, W., Zeng, A., Wei, C., Sun, Q., Yanjun, W., Pang, H. E., Mei, H., Zhang, M., Zhang, L., et al. Smplex: Scaling up expressive human pose and shape estimation. *Advances in Neural Information Processing Systems*, 36:11454–11468, 2023.

Feng, Y., Yang, J., Pollefeys, M., Black, M. J., and Bolkart, T. Capturing and animation of body and clothing from monocular video. In *SIGGRAPH Asia 2022 Conference Papers*, pp. 1–9, 2022.

Fischler, M. A. and Bolles, R. C. Random sample consensus: a paradigm for model fitting with applications to image analysis and automated cartography. *Communications of the ACM*, 24(6):381–395, 1981.

Goel, S., Pavlakos, G., Rajasegaran, J., Kanazawa, A., and Malik, J. Humans in 4d: Reconstructing and tracking humans with transformers. In *Proceedings of the IEEE/CVF International Conference on Computer Vision*, pp. 14783–14794, 2023.

Guo, C., Jiang, T., Chen, X., Song, J., and Hilliges, O. Vid2avatar: 3d avatar reconstruction from videos in the wild via self-supervised scene decomposition. In *Proceedings of the IEEE/CVF Conference on Computer Vision and Pattern Recognition*, pp. 12858–12868, 2023.

Guo, C., Li, J., Kant, Y., Sheikh, Y., Saito, S., and Cao, C. Vid2avatar-pro: Authentic avatar from videos in the wild via universal prior. In *Proceedings of the Computer Vision and Pattern Recognition Conference*, pp. 5559–5570, 2025.

Hu, L., Zhang, H., Zhang, Y., Zhou, B., Liu, B., Zhang, S., and Nie, L. Gaussianavatar: Towards realistic human avatar modeling from a single video via animatable 3d gaussians. In *Proceedings of the IEEE/CVF conference on computer vision and pattern recognition*, pp. 634–644, 2024a.

Hu, S., Hu, T., and Liu, Z. Gauhuman: Articulated gaussian splatting from monocular human videos. In *Proceedings of the IEEE/CVF conference on computer vision and pattern recognition*, pp. 20418–20431, 2024b.

Jiang, T., Chen, X., Song, J., and Hilliges, O. Instantavatar: Learning avatars from monocular video in 60 seconds. In *Proceedings of the IEEE/CVF Conference on Computer Vision and Pattern Recognition*, pp. 16922–16932, 2023.

Jiang, W., Yi, K. M., Samei, G., Tuzel, O., and Ranjan, A. Neuman: Neural human radiance field from a single video. In *European Conference on Computer Vision*, pp. 402–418. Springer, 2022.

Jung, H., Brasch, N., Song, J., Perez-Pellitero, E., Zhou, Y., Li, Z., Navab, N., and Busam, B. Deformable 3d gaussian splatting for animatable human avatars. *arXiv preprint arXiv:2312.15059*, 2023.

Kaufmann, M., Song, J., Guo, C., Shen, K., Jiang, T., Tang, C., Zárate, J. J., and Hilliges, O. Emdb: The electromagnetic database of global 3d human pose and shape in the wild. In *Proceedings of the IEEE/CVF International Conference on Computer Vision*, pp. 14632–14643, 2023.

Kerbl, B., Kopanas, G., Leimkühler, T., and Drettakis, G. 3d gaussian splatting for real-time radiance field rendering. *ACM Trans. Graph.*, 42(4):139–1, 2023.

Kinga, D., Adam, J. B., et al. A method for stochastic optimization. In *International conference on learning representations (ICLR)*, volume 5. California;, 2015.

Kirillov, A., Mintun, E., Ravi, N., Mao, H., Rolland, C., Gustafson, L., Xiao, T., Whitehead, S., Berg, A. C., Lo, W.-Y., et al. Segment anything. In *Proceedings of the IEEE/CVF international conference on computer vision*, pp. 4015–4026, 2023.

Kocabas, M., Chang, J.-H. R., Gabriel, J., Tuzel, O., and Ranjan, A. Hugs: Human gaussian splats. In *Proceedings of the IEEE/CVF conference on computer vision and pattern recognition*, pp. 505–515, 2024.

Li, M., Yao, S., Xie, Z., and Chen, K. Gaussianbody: Clothed human reconstruction via 3d gaussian splatting. *arXiv preprint arXiv:2401.09720*, 2024a.

Li, Z., Zheng, Z., Wang, L., and Liu, Y. Animatable gaussians: Learning pose-dependent gaussian maps for high-fidelity human avatar modeling. In *Proceedings of the IEEE/CVF conference on computer vision and pattern recognition*, pp. 19711–19722, 2024b.

Liu, L., Habermann, M., Rudnev, V., Sarkar, K., Gu, J., and Theobalt, C. Neural actor: Neural free-view synthesis of human actors with pose control. *ACM transactions on graphics (TOG)*, 40(6):1–16, 2021.

Loper, M., Mahmood, N., Romero, J., Pons-Moll, G., and Black, M. J. Smpl: A skinned multi-person linear model. In *Seamless Graphics Papers: Pushing the Boundaries, Volume 2*, pp. 851–866. 2023.

Mihajlovic, M., Bansal, A., Zollhoefer, M., Tang, S., and Saito, S. Keypointnerf: Generalizing image-based volumetric avatars using relative spatial encoding of keypoints. In *European conference on computer vision*, pp. 179–197. Springer, 2022.

Moon, G., Shiratori, T., and Saito, S. Expressive whole-body 3d gaussian avatar. In *European Conference on Computer Vision*, pp. 19–35. Springer, 2024.

Müller, L., Choi, H., Zhang, A., Yi, B., Malik, J., and Kanazawa, A. Reconstructing people, places, and cameras. In *Proceedings of the Computer Vision and Pattern Recognition Conference*, pp. 21948–21958, 2025.

Müller, T., Evans, A., Schied, C., and Keller, A. Instant neural graphics primitives with a multiresolution hash encoding. *ACM transactions on graphics (TOG)*, 41(4):1–15, 2022.

Pang, H., Zhu, H., Kortylewski, A., Theobalt, C., and Habermann, M. Ash: Animatable gaussian splats for efficient and photoreal human rendering. In *Proceedings of the IEEE/CVF Conference on Computer Vision and Pattern Recognition*, pp. 1165–1175, 2024.

Park, K., Sinha, U., Hedman, P., Barron, J. T., Bouaziz, S., Goldman, D. B., Martin-Brualla, R., and Seitz, S. M. Hypernerf: A higher-dimensional representation for topologically varying neural radiance fields. *arXiv preprint arXiv:2106.13228*, 2021.

Pavlakos, G., Choutas, V., Ghorbani, N., Bolkart, T., Osman, A. A., Tzionas, D., and Black, M. J. Expressive body capture: 3d hands, face, and body from a single image. In *Proceedings of the IEEE/CVF conference on computer vision and pattern recognition*, pp. 10975–10985, 2019.

Peng, S., Geng, C., Zhang, Y., Xu, Y., Wang, Q., Shuai, Q., Zhou, X., and Bao, H. Implicit neural representations with structured latent codes for human body modeling. *IEEE Transactions on Pattern Analysis and Machine Intelligence*, 45(8):9895–9907, 2023.

Qian, S., Kirschstein, T., Schoneveld, L., Davoli, D., Giebenhain, S., and Nießner, M. Gaussianavatars: Photorealistic head avatars with rigged 3d gaussians. In *Proceedings of the IEEE/CVF Conference on Computer Vision and Pattern Recognition*, pp. 20299–20309, 2024a.

Qian, Z., Wang, S., Mihajlovic, M., Geiger, A., and Tang, S. 3dgs-avatar: Animatable avatars via deformable 3d gaussian splatting. In *Proceedings of the IEEE/CVF conference on computer vision and pattern recognition*, pp. 5020–5030, 2024b.

Ravi, N., Gabeur, V., Hu, Y.-T., Hu, R., Ryali, C., Ma, T., Khedr, H., Rädl, R., Rolland, C., Gustafson, L., et al. Sam 2: Segment anything in images and videos. *arXiv preprint arXiv:2408.00714*, 2024.

Schönberger, J. L. and Frahm, J.-M. Structure-from-motion revisited. In *Conference on Computer Vision and Pattern Recognition (CVPR)*, 2016.

Schönberger, J. L., Zheng, E., Pollefeys, M., and Frahm, J.-M. Pixelwise view selection for unstructured multi-view stereo. In *European Conference on Computer Vision (ECCV)*, 2016.

Shan, W., Liu, Z., Zhang, X., Wang, S., Ma, S., and Gao, W. P-stmo: Pre-trained spatial temporal many-to-one model for 3d human pose estimation. In *European Conference on Computer Vision*, pp. 461–478. Springer, 2022.

Shao, Z., Wang, Z., Li, Z., Wang, D., Lin, X., Zhang, Y., Fan, M., and Wang, Z. Splattingavatar: Realistic real-time human avatars with mesh-embedded gaussian splatting. In *Proceedings of the IEEE/CVF Conference on Computer Vision and Pattern Recognition*, pp. 1606–1616, 2024.

Shen, K., Guo, C., Kaufmann, M., Zarate, J. J., Valentin, J., Song, J., and Hilliges, O. X-avatar: Expressive human avatars. In *Proceedings of the IEEE/CVF Conference on Computer Vision and Pattern Recognition*, pp. 16911–16921, 2023.

Triggs, B., McLauchlan, P. F., Hartley, R. I., and Fitzgibbon, A. W. Bundle adjustment—a modern synthesis. In *International workshop on vision algorithms*, pp. 298–372. Springer, 1999.

Vaswani, A., Shazeer, N., Parmar, N., Uszkoreit, J., Jones, L., Gomez, A. N., Kaiser, Ł., and Polosukhin, I. Attention is all you need. *Advances in neural information processing systems*, 30, 2017.

Wang, J., Rupprecht, C., and Novotny, D. Posediffusion: Solving pose estimation via diffusion-aided bundle adjustment. In *Proceedings of the IEEE/CVF International Conference on Computer Vision*, pp. 9773–9783, 2023.

Wang, R., Cao, Y., Han, K., and Wong, K.-Y. K. A survey on 3d human avatar modeling—from reconstruction to generation. *arXiv preprint arXiv:2406.04253*, 2024.

Wang, Z., Bovik, A. C., Sheikh, H. R., and Simoncelli, E. P. Image quality assessment: from error visibility to structural similarity. *IEEE transactions on image processing*, 13(4):600–612, 2004.

Weng, C.-Y., Curless, B., Srinivasan, P. P., Barron, J. T., and Kemelmacher-Shlizerman, I. Humannerf: Free-viewpoint rendering of moving people from monocular video. In

Proceedings of the IEEE/CVF conference on computer vision and pattern Recognition, pp. 16210–16220, 2022.

Xu, C., Tan, R. T., Tan, Y., Chen, S., Wang, X., and Wang, Y. Auxiliary tasks benefit 3d skeleton-based human motion prediction. In *Proceedings of the IEEE/CVF international conference on computer vision*, pp. 9509–9520, 2023.

Xu, Y., Chen, B., Li, Z., Zhang, H., Wang, L., Zheng, Z., and Liu, Y. Gaussian head avatar: Ultra high-fidelity head avatar via dynamic gaussians. In *Proceedings of the IEEE/CVF Conference on Computer Vision and Pattern Recognition (CVPR)*, 2024.

Xue, L., Guo, C., Zheng, C., Wang, F., Jiang, T., Ho, H.-I., Kaufmann, M., Song, J., and Hilliges, O. Hsr: holistic 3d human-scene reconstruction from monocular videos. In *European Conference on Computer Vision*, pp. 429–448. Springer, 2024.

Zhang, H., Tian, Y., Zhang, Y., Li, M., An, L., Sun, Z., and Liu, Y. Pymaf-x: Towards well-aligned full-body model regression from monocular images. *IEEE Transactions on Pattern Analysis and Machine Intelligence*, 45(10): 12287–12303, 2023.

Zhang, R., Isola, P., Efros, A. A., Shechtman, E., and Wang, O. The unreasonable effectiveness of deep features as a perceptual metric. In *Proceedings of the IEEE conference on computer vision and pattern recognition*, pp. 586–595, 2018.

Zhang, Z., Kaufmann, M., Xue, L., Song, J., and Oswald, M. R. Odhsr: Online dense 3d reconstruction of humans and scenes from monocular videos. In *Proceedings of the Computer Vision and Pattern Recognition Conference*, pp. 21824–21835, 2025.

A. Overview

This supplementary material provides further details regarding our proposed model, JOintGS. These details were omitted from the main paper due to space constraints. Furthermore, we include additional experimental results demonstrating that our model achieves State-of-the-Art (SOTA) performance in background reconstruction, even though the background was not the primary target of our optimization.

The supplementary material is organized as follows:

- SectionB: Detailed network architectures, advanced training schemes, and the loss function formulation.
- SectionC: Additional Experimental Results and Additional Demonstration Video.

B. Implementation Details

B.1. Network Architectures

We present a lightweight Multi-Layer Perceptron (MLP) network for predicting individual Gaussian properties, as illustrated in Figure S2.

Following HUGS (Kocabas et al., 2024), we employ a Tri-Plane encoding to extract spatial features for each Gaussian, which serve as input to our MLP-based decoder networks. Specifically, for a Gaussian positioned at $\mathbf{p} \in \mathbb{R}^3$, we first project it onto three orthogonal planes (XY, YZ, XZ), obtaining corresponding 2D coordinates: $\mathbf{p}_{xy}, \mathbf{p}_{yz}, \mathbf{p}_{xz}$. Utilizing bilinear interpolation, we sample the triplane feature maps at these coordinates, yielding three feature vectors: $\mathbf{f}_{xy}, \mathbf{f}_{yz}, \mathbf{f}_{xz}$. These vectors are concatenated to form the final sampling strategy spatial feature vector $\mathbf{f}_{\text{spatial}} = [\mathbf{f}_{xy}; \mathbf{f}_{yz}; \mathbf{f}_{xz}]$. To capture the temporal dynamics of human motion, we further augment the spatial feature with a time embedding, obtained by applying a positional encoding function to the time step t . Consequently, the final input feature for each Gaussian is $\mathbf{f}_{\text{input}} = [\mathbf{f}_{\text{spatial}}; \mathbf{f}_{\text{time}}]$.

We design separate Appearance and Geometry Decoders to predict distinct Gaussian attributes. The Geometry Decoder is responsible for estimating spatial properties, including mean position (μ), rotation (r), and scale (s). Conversely, the Appearance Decoder focuses on predicting visual attributes, namely color (c) and opacity (o). This architectural disentanglement enables more specialized learning and enhanced representation of geometric and appearance features.



Figure S1. Ablation study on the phased optimization schedule. From left to right: the Ground Truth reference, results of our full three-stage optimization schedule, and results of performing joint optimization only (without warm-up and independent stages).

B.2. Training Details

As introduced in the main paper (Sec. 3.5), we employ a carefully designed four-stage optimization schedule. During the Warm-up Stage, the initial learning rate is strategically set to a relatively high value. Specifically, the Gaussian attributes of the background component (μ, o, s, c, a) are assigned learning rates of 1.6×10^{-4} , 0.05, 0.005, 0.001, and 0.0025, respectively, while the foreground position (μ) and the triplane network receive learning rates of 1.6×10^{-4} and 0.001. This stage proceeds for 5,000 iterations. For computational efficiency, the Camera Optimization and Human Optimization proceed concurrently. In this parallel process, the camera pose only receives gradients originating from the background Gaussians, and the human parameters exclusively receive gradients from the foreground Gaussians. Both the camera pose

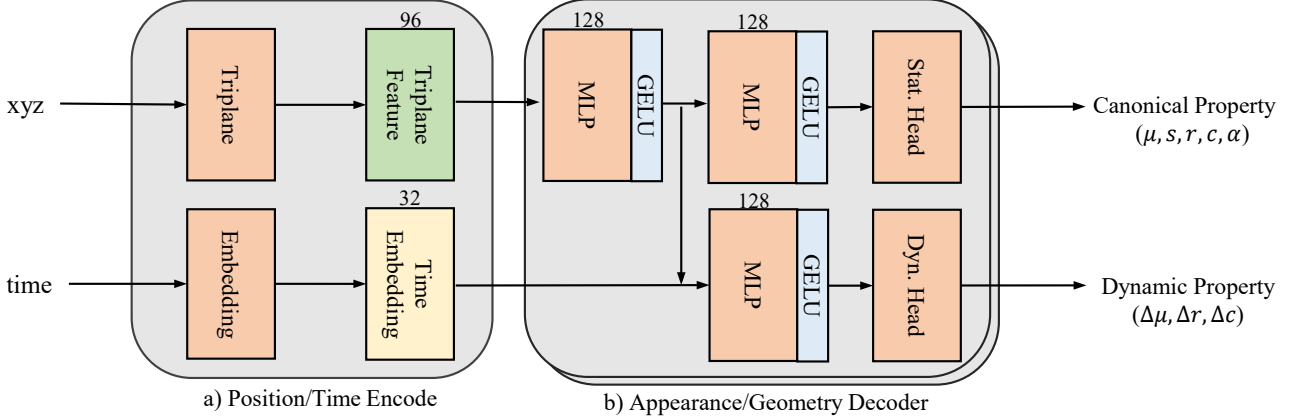


Figure S2. JOintGS Model Architecture. Our model architecture is composed of one Encoder module and two Decoder modules. In the Encoder module, the position attributes and the global temporal attributes of the Gaussian functions are encoded into positional features and temporal features, respectively. The Decoder module receives the positional features as input and utilizes a two-layer MLP with GELU activation to output either appearance or geometry features. These features are then fed into corresponding prediction heads to derive the specific attribute values. For certain dynamic attributes, we opt to inject the temporal features into the second layer of the MLP and use the same prediction head to output the corresponding residual values.

and human parameters are optimized with a learning rate of 0.001 for 5,000 iterations. To verify the necessity of this phased design, we provide an additional ablation study and visualize the results in Figure S1. The results demonstrate that skipping the initial stages and proceeding directly to joint optimization leads to severe gradient interference; specifically, a significant amount of foreground-related information is incorrectly captured by the background Gaussians. Finally, in the Joint Optimization Stage, we remove all constraints on the gradient graph, allowing the camera pose and human parameters to participate in synergistic refinement with both foreground and background Gaussians, thereby achieving the mutual correction of each component. In this stage, learning rates follow a cosine annealing schedule, decaying to 0.1 times their initial value after 10,000 iterations.

B.3. Loss Function Formulation

The overall loss is a weighted sum of three major components: rendering loss ($\mathcal{L}_{\text{render}}$), prior loss ($\mathcal{L}_{\text{prior}}$), and regularization loss ($\mathcal{L}_{\text{regular}}$):

$$\mathcal{L} = \mathcal{L}_{\text{render}} + \mathcal{L}_{\text{prior}} + \mathcal{L}_{\text{regular}} \quad (13)$$

B.3.1. RENDERING LOSS

The rendering loss, $\mathcal{L}_{\text{render}}$, represents the pixel-level fidelity between the rendered image and the ground truth. It is a combination of three metrics: \mathcal{L}_{rgb} (pixel-wise \mathcal{L}_1 loss), $\mathcal{L}_{\text{ssim}}$ (Structural Similarity Index), and $\mathcal{L}_{\text{lpips}}$ (Learned Perceptual Image Patch Similarity):

$$\mathcal{L}_{\text{render}} = \lambda_{\text{rgb}} \mathcal{L}_{\text{rgb}} + \lambda_{\text{ssim}} \mathcal{L}_{\text{ssim}} + \lambda_{\text{lpips}} \mathcal{L}_{\text{lpips}} \quad (14)$$

We set the corresponding weights as $\lambda_{\text{rgb}} = 1$, $\lambda_{\text{ssim}} = 0.4$, and $\lambda_{\text{lpips}} = 0.2$.

B.3.2. PRIOR LOSS

The prior loss, $\mathcal{L}_{\text{prior}}$, incorporates prior knowledge into the optimization process, specifically ensuring the rendered human avatar adheres to a segmentation mask:

$$\mathcal{L}_{\text{prior}} = \lambda_{\text{mask}} \mathcal{L}_{\text{mask}} \quad (15)$$

Here, $\mathcal{L}_{\text{mask}}$ is the Mean Squared Error (MSE) loss between the rendered human body segmentation and the provided prior mask. The weight for this term is $\lambda_{\text{mask}} = 0.01$.

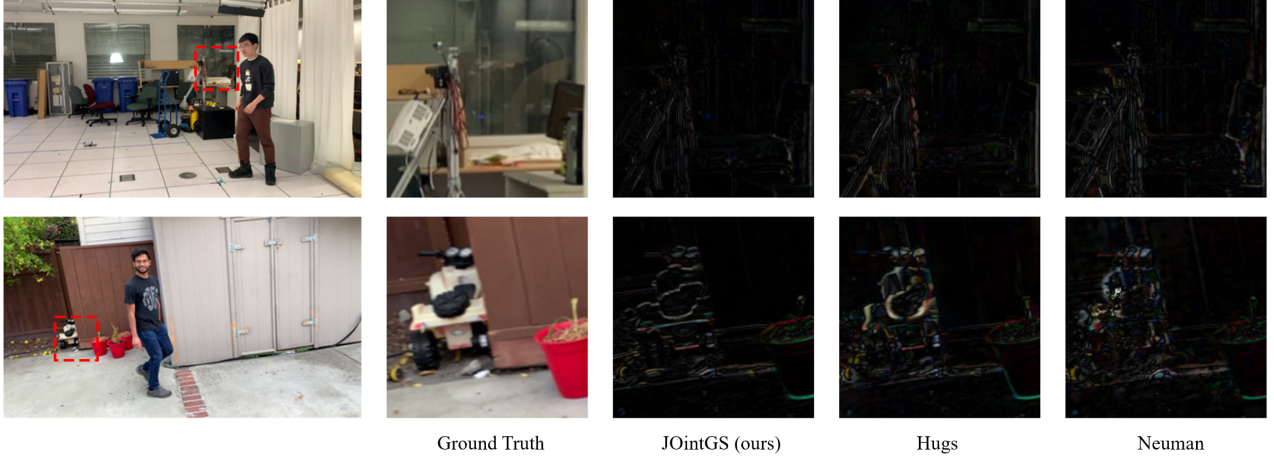


Figure S3. Qualitative comparison on NeuMan dataset. For each scene, we present the complete rendered image (first column) and a zoomed-in view of a densely textured region (second column), along with the error map of different methods (last three columns).

B.3.3. REGULARIZATION LOSS

The regularization term, $\mathcal{L}_{\text{regular}}$, is introduced to maintain model stability and geometric plausibility, encompassing Linear Blend Skinning (LBS) constraints, geometric constraints with the SMPL model, and dynamic attribute regularization:

$$\mathcal{L}_{\text{regular}} = \lambda_{\text{lbs}} \mathcal{L}_{\text{lbs}} + \lambda_{\text{smpl}} \mathcal{L}_{\text{smpl}} + \lambda_{\text{dyn}} \mathcal{L}_{\text{dyn}} \quad (16)$$

The term $\mathcal{L}_{\text{smpl}}$ is the \mathcal{L}_1 loss measuring the deviation of foreground Gaussian points from the reconstructed SMPL surface. \mathcal{L}_{dyn} is the \mathcal{L}_2 loss applied to all dynamic attributes predicted by the deformation network. We use the following weights: $\lambda_{\text{lbs}} = 20$, $\lambda_{\text{smpl}} = 0.005$, and $\lambda_{\text{dyn}} = 0.01$.

	Seattle			Citron			Parking			Bike			Jogging			Lab		
	PSNR \uparrow	SSIM \uparrow	LPIPS \downarrow	PSNR \uparrow	SSIM \uparrow	LPIPS \downarrow	PSNR \uparrow	SSIM \uparrow	LPIPS \downarrow	PSNR \uparrow	SSIM \uparrow	LPIPS \downarrow	PSNR \uparrow	SSIM \uparrow	LPIPS \downarrow	PSNR \uparrow	SSIM \uparrow	LPIPS \downarrow
Vid2Avatar (Guo et al., 2023)	16.90	0.51	0.27	15.96	0.59	0.28	18.51	0.65	0.26	12.44	0.39	0.54	16.36	0.46	0.30	15.99	0.62	0.34
NeuMan (Jiang et al., 2022)	18.42	0.58	0.20	18.39	0.64	0.19	17.66	0.66	0.24	19.05	0.66	0.21	17.57	0.54	0.29	18.76	0.73	0.23
HUGS (Kocabas et al., 2024)	19.06	0.67	0.15	19.16	0.71	0.16	19.44	0.73	0.17	19.48	0.67	0.18	17.45	0.59	0.27	18.79	0.76	0.18
JOintGS (Ours)	25.13	0.88	0.08	25.39	0.87	0.10	24.70	0.86	0.17	25.21	0.85	0.16	21.77	0.77	0.16	25.30	0.87	0.14

Table S1. Human reconstruction quality on NeuMan dataset. Quantitative comparison on human-only regions cropped using tight bounding boxes. Our method achieves state-of-the-art performance across all six sequences

	Seattle			Citron			Parking			Bike			Jogging			Lab		
	PSNR \uparrow	SSIM \uparrow	LPIPS \downarrow	PSNR \uparrow	SSIM \uparrow	LPIPS \downarrow	PSNR \uparrow	SSIM \uparrow	LPIPS \downarrow	PSNR \uparrow	SSIM \uparrow	LPIPS \downarrow	PSNR \uparrow	SSIM \uparrow	LPIPS \downarrow	PSNR \uparrow	SSIM \uparrow	LPIPS \downarrow
HyperNeRF (Park et al., 2021)	16.43	0.43	0.40	16.81	0.41	0.56	16.04	0.38	0.62	17.64	0.42	0.43	18.52	0.39	0.52	16.75	0.51	0.23
Vid2Avatar (Guo et al., 2023)	17.41	0.56	0.60	14.32	0.62	0.65	21.56	0.69	0.50	14.86	0.51	0.69	15.04	0.41	0.70	13.96	0.60	0.68
NeuMan (Jiang et al., 2022)	23.99	0.78	0.26	24.63	0.81	0.26	25.43	0.80	0.31	25.55	0.83	0.23	22.70	0.68	0.32	24.96	0.86	0.21
HUGS (Kocabas et al., 2024)	25.94	0.85	0.13	25.54	0.86	0.15	26.86	0.85	0.22	25.46	0.84	0.13	23.75	0.78	0.22	26.00	0.92	0.09
JOintGS (Ours)	32.52	0.95	0.04	26.27	0.84	0.09	32.77	0.92	0.09	31.19	0.94	0.04	28.29	0.89	0.11	30.35	0.94	0.06

Table S2. Full-image reconstruction quality assessment on the NeuMan dataset. Evaluation is conducted on the entire frames without any region-specific cropping or masking.

C. Supplementary Experiments

C.1. Per-Scene Experimental Results

We provide a comprehensive scene-by-scene performance comparison on the NeuMan dataset, as detailed in Table S1 and Table S2. To offer a multi-faceted evaluation, we report metrics under two distinct settings. First, Table S1 presents the results calculated exclusively within the **human-only regions**, which are cropped using tight bounding boxes for each sequence to directly reflect the fidelity of our human reconstruction. Second, Table S2 provides the evaluation on the **entire images** to assess the overall scene reconstruction quality, including the background.

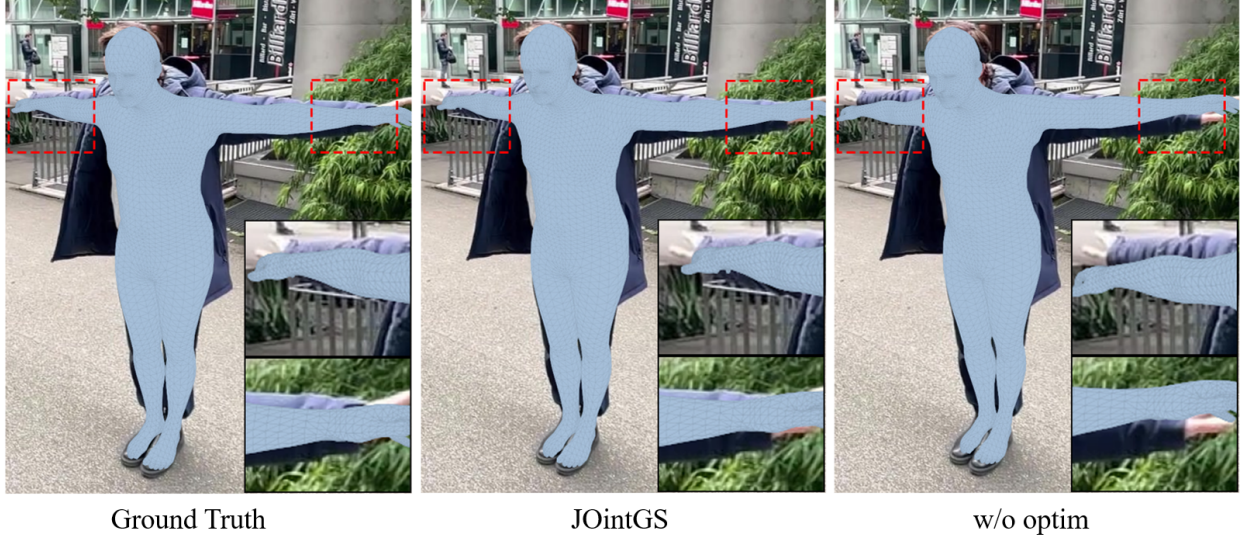


Figure S4. Qualitative comparison of SMPL pose refinement. We overlay the estimated 3D human meshes onto the ground truth images to evaluate spatial alignment. From left to right: (Left) The reference image with ground truth pose; (Middle) Results after our JOintGS optimization; (Right) Results without optimization (initial estimates).

Both quantitative evaluations employ standard photometric metrics (PSNR, SSIM (Wang et al., 2004), and LPIPS (Zhang et al., 2018)) as defined in §4.1. As shown in these results, our approach consistently outperforms existing SOTA methods across various complex scenes. Visual results in Figure S3 further confirm that our model achieves superior spatial alignment and texture detail for both the foreground human and the static background.

C.2. Visualization of Human Pose Optimization

Beyond pixel-level photometric evaluations, we further assess the effectiveness of our joint optimization by visualizing the refinement of human pose parameters. In Figure S4, we overlay the estimated 3D human meshes onto the ground truth images to qualitatively evaluate the spatial alignment.

It is evident that our method successfully corrects significant misalignments present in the initial poses. Quantitatively, our joint optimization reduces the Mean Per-Joint Position Error (MPJPE) by 4mm compared to the initial estimates. As shown in the middle column of Figure S4, our optimized results demonstrate precise alignment with the image evidence, whereas the unoptimized initial estimates (right column) exhibit noticeable deviations from the actual human contours. By iteratively refining the body pose $\{\theta_t, \beta\}$ in tandem with camera trajectories, our model achieves superior geometric precision. This accurately aligned pose provides a stable and consistent anchor for the Gaussian attributes, thereby ensuring the temporal coherence of the reconstructed human avatars.

C.3. Demonstration Video

We provide a demonstration video on our GitHub project page to visually showcase the high fidelity of our reconstruction. The video includes extensive results for both novel-view and novel-pose synthesis, confirming the effectiveness of our approach in modeling dynamic human bodies within the scene.